applied nano

MDPI

Article

# Effect of the Cross-Section Morphology in the Antimicrobial Properties of α-$Ag_2WO_4$ Rods: An Experimental and Theoretical Study

**Nivaldo F. Andrade Neto [1], Marisa C. Oliveira [2], José Heriberto O. Nascimento [3], Elson Longo [2], Renan A. P. Ribeiro [4,*], Mauricio R. D. Bomio [1] and Fabiana V. Motta [1]**

1 Laboratory of Chemical Synthesis of Materials, Department of Materials Engineering, Federal University of Rio Grande do Norte—UFRN, Natal P.O. Box 1524, RN, Brazil
2 Department of Chemistry, Functional Materials Development Center, Federal University of São Carlos-UFSCar, São Carlos P.O. Box 676, SP, Brazil
3 Laboratory of Textile Chemical Process, Department of Textile Engineering, Federal University of Rio Grande do Norte—UFRN, Natal P.O. Box 1524, RN, Brazil
4 Laboratory of Theoretical Chemistry and Computational Modeling, Department of Natural and Earth Sciences, Minas Gerais State University—UEMG, Av. Paraná, 3001, Divinópolis 35501-170, MG, Brazil
* Correspondence: ribeiroapr@gmail.com or renan.ribeiro@uemg.br; Tel.: +55-37-3229-3558

**Abstract:** In this work, α-$Ag_2WO_4$ particles with different cross-sections were obtained using the co-precipitation method at different synthesis temperatures. The samples were characterized by X-ray diffraction (XRD), field-scanning electron microscopy (SEM), and X-ray photoelectron spectroscopy (XPS). The antimicrobial activity was analyzed using the Minimum Inhibitory Concentration (MIC) and Minimum Bactericidal Concentration (MBC) methods against the *Escherichia coli* and *Salmonella* spp. gram-negative bacteria. The antimicrobial tests against *Escherichia coli* and *Salmonella* spp. indicated that concentrations of 2.5–5 mg/mL and 5 mg/mL completely inhibit its growth, respectively. The antimicrobial activity was analyzed employing band-edge positions for ROS generations and the superficial distribution of $Ag^+$ species that contribute to antimicrobial activity. Quantum-chemical calculations were used at the DFT level to investigate the surface-dependent reactivity of α-$Ag_2WO_4$, and we demonstrated how the antimicrobial properties could be tailored by the geometry and electronic structure of the exposed surfaces, providing guidelines for the morphology design.

**Keywords:** α-$Ag_2WO_4$; cross-section; antimicrobial activity; ROS generation; theoretical study

check for updates

**Citation:** Andrade Neto, N.F.; Oliveira, M.C.; Nascimento, J.H.O.; Longo, E.; Ribeiro, R.A.P.; Bomio, M.R.D.; Motta, F.V. Effect of the Cross-Section Morphology in the Antimicrobial Properties of α-$Ag_2WO_4$ Rods: An Experimental and Theoretical Study. *Appl. Nano* **2023**, *4*, 213–225. https://doi.org/10.3390/applnano4030012

Academic Editors: Anthony William Coleman and Giacomo Dacarro

Received: 8 March 2023
Revised: 10 July 2023
Accepted: 18 July 2023
Published: 31 July 2023



## 1. Introduction

Diseases caused by microbes are a global problem, and it is even more severe in underdeveloped countries due to lack of hygiene or even proper treatment [1,2]. In addition, treating microbes with conventional remedies results in making them more resistant over time, and it is increasingly necessary to use stronger medications for the treatment to promote the expected result [3,4]. Metallic oxide particles are a well-recognized strategy because they are toxic to microbes, but present low toxicity to humans [5–7]. The use of semiconductor oxides enables the manipulation of their properties by increasing the separation process of electron/hole charge pairs ($e^-/h^+$), which enhances the formation of reactive oxygen species (ROS), such as hydroxyl radical ($^{\bullet}OH$) and superoxide radical ($^{\bullet}O_2^-$), that degrade the constituent proteins and membranes of the microorganisms [8].

Our research group and other authors have been involved in a research field in which complex silver-based oxides, such as $Ag_2CrO_4$ [9,10], the three polymorphs of $Ag_2WO_4$ [11–14], $Ag_3PO_4$ [15,16], α-$AgVO_3$ [17], and β-$Ag_2MoO_4$ [18–21], are investigated as biocide materials. α-$Ag_2WO_4$ becomes even more interesting because it absorbs a large amount of radiation in the visible region and has optoelectronic properties closely related to particle size, allowing for better control [11,12,22–27].

In this work, nanoparticles of α-$Ag_2WO_4$ with rod morphology were obtained by a co-precipitation method. The cross-section of the rods was changed from hexagonal to quadratic through an increase in the synthesis temperature from 30 to 70 °C. The cross-section effect in the antimicrobial properties was analyzed against *Escherichia coli* and *Salmonella* spp. In addition, DFT calculations, on realistic surface models, were carried out to investigate the geometry, electronic structure, and properties of α-$Ag_2WO_4$. Based on these results, we hope to understand how the different surfaces change their energies throughout the synthesis process and propose a mechanism by which the experimental and theoretical morphologies of the α-$Ag_2WO_4$ perform the antimicrobial activity more efficiently. We believe that these novel results are of significant relevance since they may inspire the efficient synthesis of this material and provide critical information to expand our fundamental understanding of this property in this compound.

## 2. Experimental Procedure

### *2.1. Synthesis*

Silver nitrate ($AgNO_3$—Synth, 99%), sodium tungstate ($Na_2WO_4 \cdot 2H_2O$—Synth, 99.5%), polyvinylpyrrolidone (PVP—Vetec, MM. 40.000), and deionized water were used as received.

Firstly, 4 mmol of $AgNO_3$ and 10 mmol of PVP were dumped in 40 mL of deionized water and in a glass beaker and continuously stirred. Then, 2 mmol of $Na_2WO_4 \cdot 2H_2O$ and 10 mmol of PVP were dissolved in 40 mL of deionized water in another glass beaker. After 10 min, the solution containing $Ag^+$ cations was immersed in the $W^{6+}$ solution and was maintained under vigorous stirring for 30 min at 30 °C (AW30 sample). The same procedure was repeated, increasing the precipitation temperature to 70 °C (AW70 sample). After 30 min, the supernatant was separated by centrifugation, washed with deionized water, and dried at 100 °C for 24 h.

### *2.2. Characterization*

The crystalline phase of the powder was analyzed by X-ray diffraction using CuKα radiation (1.5418 Å), scanning from 10 to 80°, using a speed of 1°/min and a step of 0.02° in a Shimadzu diffractometer (XRD-6000). Rietveld refinement was performed in the General Structure Analysis System (GSAS) program (Developed by the Advanced Photon Source, Argonne National Laboratory, Developed by the Advanced Photon Source, Argonne National Laboratory, Lemont, IL, USA) with a EXPGUI graphical interface version 1166 [28] using background, scale factor, microstructure, crystal, texture, and strain parameters for refinement. The α-$Ag_2WO_4$ rods morphology was observed by a field emission scanning electron microscope (FE-SEM, Carl-Zeiss—microscope, ZEISS Microscopy, Oberkochen, Germany). X-ray photoelectron spectroscopy (XPS) was performed in a ESCALAB 250Xi (Thermo Fisher Scientific, Waltham, MA, USA) device operating with AlKα (hν = 1486.68 eV) radiation at 225 W and 15 kV. The XPS spectra were collected at 200 eV and 20 eV for survey spectra and individual elements, respectively.

### *2.3. Antimicrobial Tests*

The α-$Ag_2WO_4$ powders' antimicrobial capacity was analyzed using the Minimum Inhibitory Concentration (MIC) and Minimum Bactericidal Concentration (MBC) methods.

Minimal inhibitory concentration (MIC) of the α-$Ag_2WO_4$ powders was determined using the broth microdilution method [29] with modifications using 96-well microtiter plates. The pre-inoculum culture consisted of a bacterial colony cultivated in 5 mL Muller–Hinton medium (MH) at 37 °C for 16–18 h under 180 rpm agitation. After this period, 5 µL of pre-inoculum was transferred to 5 mL of MH and incubated at 37 °C with agitation until optical density reached 0.1 at 600 nm measured by UV-VIS (Quant, Biotek, American Laboratory Trading, San Diego, CA, USA). The α-$Ag_2WO_4$ samples were firstly dissolved in sterile distilled water and added to the MH medium for a final dose of 5 µg/mL. The samples were serially diluted, and 50 µL was added to each well. The bacterial inoculums were adjusted to $10^6$ CFU/mL concentration and inoculated with samples and MH at

a final volume of 100 μL/well. The plates were incubated at 37 °C for 16–20 h with no agitation. MIC was considered as the lowest concentration which inhibited visual growth. Next, an aliquot of each growth well content was inoculated in an MH agar plate and incubated at 37 °C for 24 h for the Minimum Bactericidal Concentration (MBC) test. MBC was considered as the lowest concentration at which no bacterial colonies were observed. The bacteria used were gram-negative *Escherichia coli* and *Salmonella spp*. Negative and sterility controls were included, and all experiments were performed in triplicate.

### *2.4. Computational Details*

Computational methods and theoretical procedures were employed to study the bulk and surfaces related to $\alpha$-$Ag_2WO_4$. Density Functional Theory (DFT) calculations were carried out using the periodic ab initio CRYSTAL17 [30] package within B3LYP [31,32] hybrid functional. This computational technique has been successfully applied to study the electronic and structural properties of various Ag-based materials [33–37]. The Ag and W atoms in all calculations were described using effective core pseudopotential HAYWSC-311d31G and HAYWSC-11d31G, respectively, while O atoms were described using atom-centered all-electron Gaussian basis 8-411G [38–40]. Low-index (100), (001), (001) and (101) slab models were employed in order to evaluate the physical and chemical properties associated with $\alpha$-$Ag_2WO_4$ surfaces. Herein, the previous optimized surface models [11,41] obtained combining semi-local PBE exchange-correlation functional and plane-wave basis set were considered as first guess for electronic structure analysis with atom-centered basis set and a hybrid functional approach. The electronic structure analysis was carried out combining band-edge positions, electrostatic potential isosurfaces, and surface-dependent chemical environment from undercoordinated cations.

## 3. Results and Discussion

The diffractograms for the $Ag_2WO_4$ powders obtained at 30 and 70 °C are shown in Figure 1a,b, respectively. According to diffractograms, all peaks corresponding to the alpha phase of the silver tungstate, which have an orthorhombic system and space group P2n2 (no. 34), are characterized by the ICSD 243987 card. The absence of secondary peaks indicates that the co-precipitation method at different temperatures is efficient for the $\alpha$-$Ag_2WO_4$ phase obtention. The ICSD 243987 card was used for Rietveld refinement in the GSAS software and Table 1 shows the obtained data. According to data obtained by the refinement, the increase in the precipitation temperature provided a little increase in the crystallite size, followed by a reduction in the microstrain. The growth of crystallites occurred due to the increase in the lattice parameters of the material, as shown in Table 1. These changes occurred because of the greater energy during the synthesis procedure, enabling the greater lattice accommodation and energy reduction associated with crystallites. Table S1 shows the fractional coordinates of the atoms, indicating that the increase in temperature favors the displacement of the atoms, facilitating their accommodation in the crystalline lattice. The low values of the refinement coefficients, in parallel with the good fit between the theoretical and practical diffractograms, indicate the reliability of the data obtained by the refinement.

Figure 1c,d show the micrographs for the AW30 and AW70 samples, respectively. The growth of particles in well-defined morphologies can be explained by the energy associated with the surface planes. According to the highlighted images, it is clear that the temperature increase changed the cross-section of the rods, changing them from hexagonal to square form. Roca et al. [42] showed the possible morphologies of $\alpha$-$Ag_2WO_4$ through DFT calculations using the Wulff construction obtained by a microwave-assisted hydrothermal method and according to the surface energy of the crystallographic planes. According to this study, the markings 1, 2, 3, and 4 refer to the (010), (001), (101), and (100) planes. Therefore, we suggest that the rods obtained in this work at 30 °C preferentially grow in the [010] direction, while the increase in precipitation temperature to 70 °C favors growth in the [100] direction. The increase in precipitation temperature provides greater energy

to the system, allowing the growth of particles in a morphology which has less energy associated with its crystallographic planes. As seen through the diffractograms, α-$Ag_2WO_4$ has an orthorhombic crystalline structure, justifying the growth of the particles in the [100] direction when increasing the precipitation temperature.

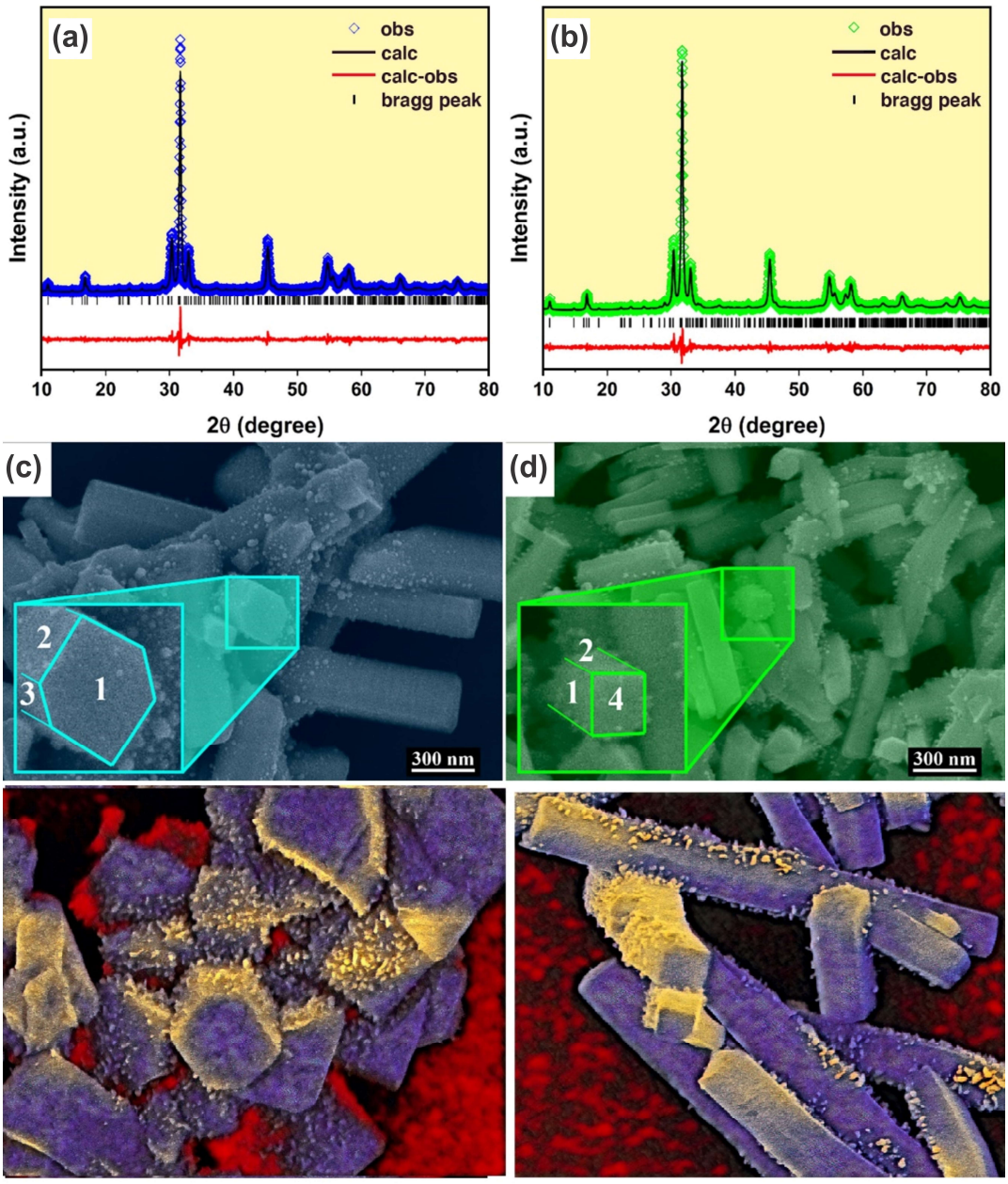


**Figure 1.** (**a**,**b**) Diffractograms and (**c**,**d**) SEM images highlighting the morphology and growth plans for AW30 and AW70 samples, respectively. Where numbers 1, 2, 3, and 4 refer to (010), (001), (101), and (100) planes.

The chemical environment for (100), (010), (001), and (101) surfaces were analyzed based on the Wulff construction [42], as presented in the Figure 2. In this case, the (100) surface exposed a 5-fold Ag and W center, while (010) exposed a 4-fold Ag-center. On the other hand, the (001) and (101) surfaces exhibited $Ag_{5c}$ and $Ag_{4c}$ centers summed to $W_{5c}$ (101) and $W_{4c}$ (001). Therefore, the (100) and (010) surfaces showed a more regular environment in comparison to the (001) and (101) surfaces that presented a higher undercoordinated degree.

**Table 1.** Refinement data obtained by the GSAS software (EXPGUI graphical interface version 1166).

| Samples | AW30 | AW70 |
|---|---|---|
| Crystallite size (nm) | 24.8 | 25.1 |
| Microstrain ($\times 10^{-4}$) | 4.04 | 4.00 |
| *a* (Å) | 10.874(9) | 10.875(0) |
| *b* (Å) | 12.000(7) | 12.002(7) |
| *c* (Å) | 5.896(3) | 5.897(3) |
| Vollum (Å$^3$) | 769.505(0) | 769.770(8) |
| Chi$^2$ | 1.292 | 1.31 |
| Wrp (%) | 9.99 | 10.36 |
| Rp (%) | 7.86 | 8.06 |

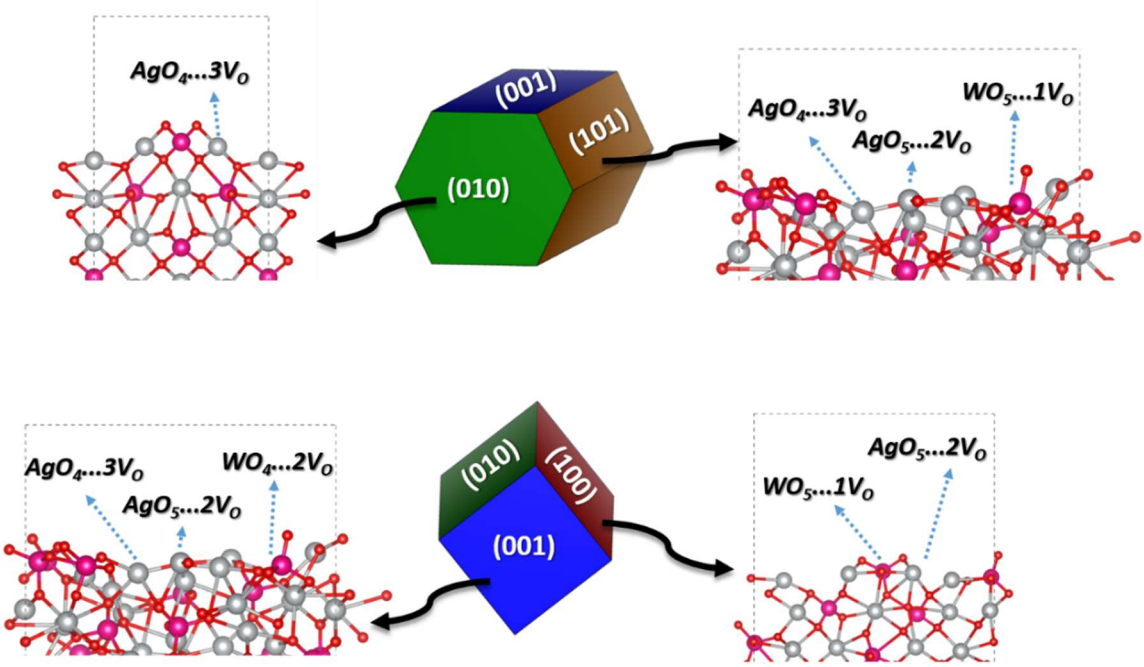


**Figure 2.** Schematic representation of (100), (010), (001), and (101) surfaces of $\alpha$-$Ag_2WO_4$.

Figure 3 shows the XPS spectra for the AW70 sample. According to Figure 3b, Ag 3d had two peaks at 367.2 and 373.2 eV, which could be assigned to Ag $3d_{5/2}$ and Ag $3d_{3/2}$, respectively. These peaks were ascribed to $Ag^+$ and the absence of minor peaks after deconvolution of these peaks indicated the non-formation of metallic silver ($Ag^0$) [43]. The high-resolution spectra for W 4f are shown in Figure 3c. The peaks at 34.1 and 36.3 eV correspond to W $4f_{7/2}$ and W $4f_{5/2}$, respectively, relative to $W^{6+}$ [44]. Figure 3d shows the deconvolution of the O 1s peak in two, 529.5 and 530.7 eV, which can be attributed to lattice oxygen and the oxygen of water molecules adsorbed on the surface, respectively [45].

The antimicrobial capacity of the $\alpha$-$Ag_2WO_4$ powders was estimated by MIC and MBC methods. Table 2 shows the methodology of presentation of the inhibitory results, and Tables 3 and 4 show the results against *Escherichia coli* and *Salmonella* spp. according to the plates shown in Figures S1 and S2 (Supplementary Materials). The negative control refers to a well without $\alpha$-$Ag_2WO_4$ samples, while the sterility controls refer to a well without bacteria or $\alpha$-$Ag_2WO_4$. According to Tables 3 and 4, the growth in all wells in columns 8 and 9, and the non-growth in the wells in columns 10 and 11, indicate the correct sterilization during the preparation process, indicating the reliability of the results. The results against *E. coli* indicate that the 5 and 2.5 mg/mL concentrations of AW30 and AW70 samples inhibited the growth of the bacteria, while lower concentrations did not hinder them. On the other hand, only 5 mg/mL concentration against *Salmonella* spp. resulted in the inhibition of bacterial growth for the AW30 and AW70 samples.

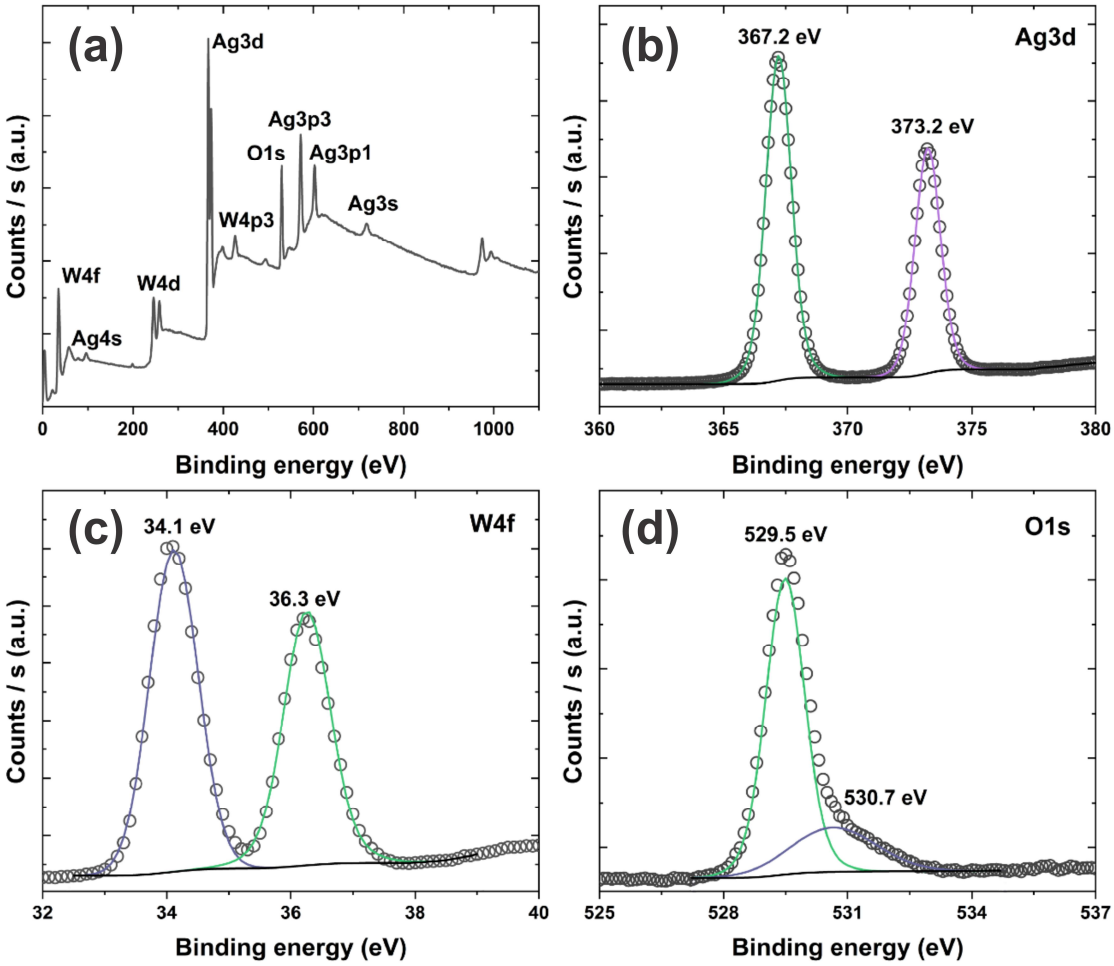


**Figure 3.** (**a**) XPS spectra for the AW70 sample and high-resolution spectra for the (**b**) Ag3d, (**c**) W4f, and (**d**) O1s element states. Green lines correspond to Ag $3d_{5/2}$, W $4f_{5/2}$ and $O_{lattice}$ in (**b**–**d**), respectively. Purple lines correspond to Ag $3d_{3/2}$, W $4f_{7/2}$ and $O_{water}$ in (**b**–**d**), respectively.

**Table 2.** Presentation of antimicrobial results, where C1 to C7 refer to concentrations of 5, 2.5, 1.25, 0.625, 0.3125, 0.156, and 0.078 mg/mL, respectively. NC and SC are negative and sterility controls, respectively.

| | 1 | 2 | 3 | 4 | 5 | 6 | 7 | 8 | 9 | 10 | 11 |
|---|---|---|---|---|---|---|---|---|---|---|---|
| AW30 | C1 | C2 | C3 | C4 | C5 | C6 | C7 | NC | NC | SC | SC |
| | C1 | C2 | C3 | C4 | C5 | C6 | C7 | NC | NC | SC | SC |
| | C1 | C2 | C3 | C4 | C5 | C6 | C7 | NC | NC | SC | SC |
| AW70 | C1 | C2 | C3 | C4 | C5 | C6 | C7 | NC | NC | SC | SC |
| | C1 | C2 | C3 | C4 | C5 | C6 | C7 | NC | NC | SC | SC |
| | C1 | C2 | C3 | C4 | C5 | C6 | C7 | NC | NC | SC | SC |

**Table 3.** Inhibition of *Escherichia coli*, where (+) and (−) correspond to growth and inhibition, respectively.

| | 1 | 2 | 3 | 4 | 5 | 6 | 7 | 8 | 9 | 10 | 11 |
|---|---|---|---|---|---|---|---|---|---|---|---|
| AW30 | − | − | + | + | + | + | + | + | + | − | − |
| | − | − | − | + | + | + | + | + | + | − | − |
| | − | − | + | + | + | + | + | + | + | − | − |
| AW70 | − | − | + | + | + | + | + | + | + | − | − |
| | − | − | + | + | + | + | + | + | + | − | − |
| | − | − | − | + | + | + | + | + | + | − | − |

**Table 4.** Inhibition of *Salmonella* spp., where (+) and (−) correspond to growth and inhibition, respectively.

| | 1 | 2 | 3 | 4 | 5 | 6 | 7 | 8 | 9 | 10 | 11 |
|---|---|---|---|---|---|---|---|---|---|---|---|
| AW30 | − | + | + | + | + | + | + | + | + | − | − |
| | − | + | + | + | + | + | + | + | + | + | + |
| | − | + | + | + | + | + | + | + | + | − | − |
| AW70 | − | + | + | + | + | + | + | + | + | − | − |
| | + | − | + | + | + | + | + | + | + | − | − |
| | − | + | + | + | + | + | + | + | + | + | − |

From now on, our major interest is devoted to explaining the antimicrobial capacity of the $\alpha$-$Ag_2WO_4$ powders based on electronic structure analysis. It is well known that Ag-based semiconductors can exhibit superior antimicrobial activity due to their capability of generating ROS from $O_2$ adsorption, activation, and evolution along with the exposed surfaces [11,13,46,47]. In addition, other authors argue that the presence of exposed $Ag^+$ ions are toxic and are able to kill the bacteria through the denaturation or oxidation mechanism [48,49]. In both cases, morphological modulations seem to be the best alternative to tailor the biological activity and provide superior behaviors.

In this context, Ag- and Cu-based nanoparticles have recently had their interest renewed, as experimental results indicate the antiviral potential of semiconductor materials against SARs-CoV-2 virus, also known as COVID-19 [8,50–52]. In particular, ROS generation summed to the metal-rich surface exposure induces the superior biological activity of such materials, contributing to designing innovative materials and reducing the drastic effects of COVID-19 and similar pathogens. Moreover, theoretical results have also confirmed the role of surface exposure to provide superior ROS generation, indicating that the rational design of solid-state materials plays a key role in present and future medical applications [53–56].

Aiming to complement such discussion, the vacuum band-edge positions were computed using the expressions:

$$E_{CB} = \chi - E^e - \frac{1}{2}E_{gap} \quad (1)$$

$$E_{VB} = E_{CB} + E_{gap} \quad (2)$$

in which $E_{CB}$ and $E_{VB}$ correspond to the *VB* and *CB* potential, $E^e$ is the energy of free electrons vs. hydrogen electrode potential (NHE = 4.5 eV) [57], $\chi$ is the Mulliken electronegativity calculated as 5.989 eV for $\alpha$-$Ag_2WO_4$, and $E_{gap}$ is the band-gap value estimated here by DFT calculations. In this context, it is important to mention that the calculated band-gap values showed good agreement with the experimental data for AW30 and AW70 (Figure S3—Supplementary Materials), where the role of exposed surfaces explain the reduced band-gap values in comparison with the bulk. Figure 4 exhibits the band edge potential for bulk and surfaces of $\alpha$-$Ag_2WO_4$ with respect to NHE. In order to verify if the bulk and different surfaces of $\alpha$-$Ag_2WO_4$ are capable of generating ROS species, i.e., hydroxyl ($^{\bullet}OH$) and superoxide radicals ($^{\bullet}O_2^-$), from adsorbed $H_2O$ and $O_2$ molecules, it is possible to compare the *VB*/*CB* position with the potential of $H_2O/^{\bullet}OH$ and $O_2/^{\bullet}O_2^-$ reactions, respectively, at different pH levels, such as 0 and 7.

According to Figure 4, the position of VB shows that the bulk and surface models of $\alpha$-$Ag_2WO_4$ can be used to generate $^{\bullet}OH$ radicals from $H_2O$ oxidation at pH = 0, since the VBM are more positive than the redox potential +1.23 V for $H_2O/^{\bullet}OH$ versus NHE. Only the (101) cannot be used to generate $^{\bullet}OH$ radical at pH = 7, since the VBM is more negative that the redox potential of +2.72 V (NHE). With regard to the reduction reaction involving adsorbed oxygen species $O_2/^{\bullet}O_2^-$, only the CB positions for the bulk and (010) surfaces are properly able to active the adsorbed species and generate $^{\bullet}O_2^-$, since the CB values are higher than the redox potential of −0.33 V (NHE).

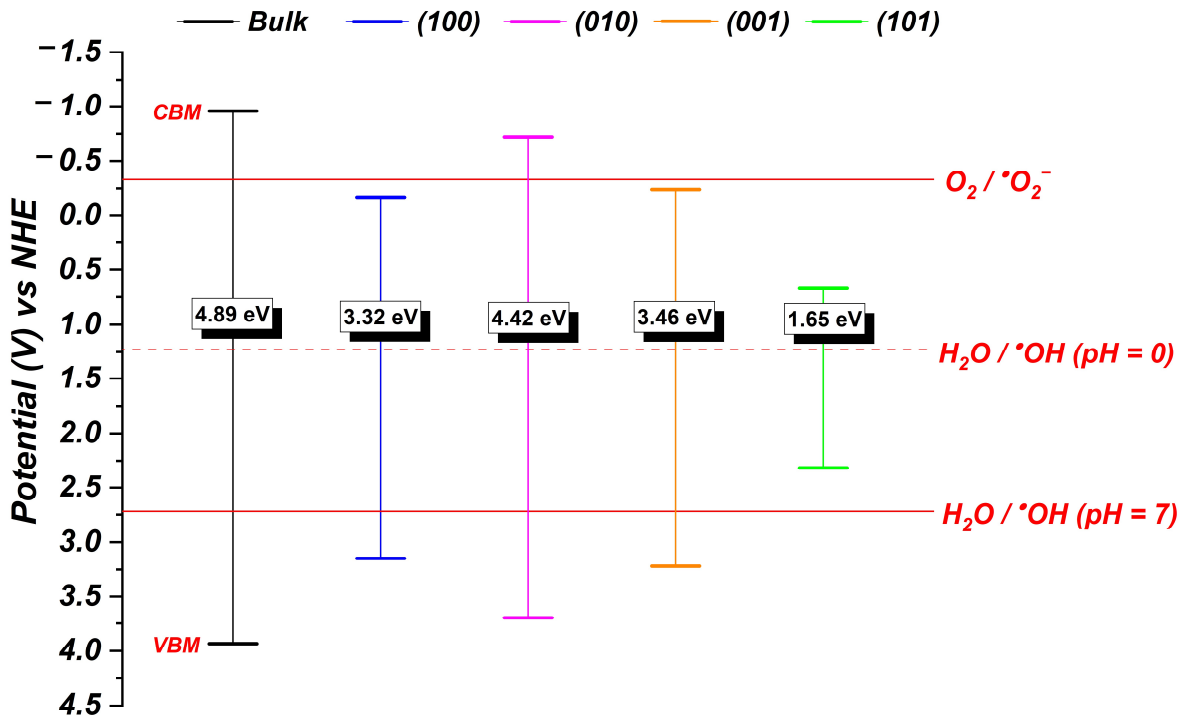


**Figure 4.** Band-edge values for bulk and surfaces models of $\alpha$-$Ag_2WO_4$ with respect to hydrogen electrode potential (NHE).

Based on these results, we can argue that the bulk and (010) surfaces band-edge potential of $\alpha$-$Ag_2WO_4$ are the most favorable in provoking the formation of ROS considering both oxidative and reductive reactions, being that the VBM and CBM potential, associated with the superficial chemical environment represented in Figure 2, contributes as hole-trapping centers which activate adsorbed $H_2O$ and $O_2$ species to generate $^{\bullet}OH$ and $^{\bullet}O_2{}^{-}$, respectively. Moreover, we can argue that all investigated surfaces of $\alpha$-$Ag_2WO_4$ contribute to generate at least one type of ROS ($^{\bullet}OH$) that help us to explain the biological activity reported in this work and by previous experimental results [12,13,24,26,47].

Very recently, our research group proposed a new concept to describe the atomic coordination environment of surface atoms. We found a relationship between the material properties (biological and catalytic behavior) and the exposed surface at the morphology, as well as finding that the ROS generation in the $\alpha$-$Ag_2WO_4$, $\beta$-$Ag_2MoO_4$, and $Ag_2CrO_4$ [9,21,58] was sustained. On the other hand, the reactivity and antimicrobial behavior of shape-oriented $Ag_2O$ nanoparticles were attributed to the presence of (100) surfaces with increased distribution of $Ag^+$ species [48,49,59]. Moreover, the electrostatic potential isosurface contributes to depicting the charge density distribution to describe the reactivity of exposed surfaces in the morphology of different materials [60,61]. Therefore, the calculated charge density distributions for $\alpha$-$Ag_2WO_4$ surfaces are shown in Figure 5.

An analysis of the results point out that the (001) and (101) surfaces exhibit a large positive charge concentration, while (100) and (010) show the presence of negative and positive charge centers along the exposed surfaces. In addition, we can interpret that the most positive surfaces induce reduced formation energy for Ag vacancies, contributing to $Ag^+$ release. Therefore, the (001) and (101) can attach to the bacteria membrane and release $Ag^+$ cations that contribute to oxidative stress and cell death.

Moreover, the electrostatic potential surface and band-edge positions can be combined to understand the activation process of adsorbed $H_2O$ and $O_2$ in ROS generation. The more positive surfaces exhibit a metal-rich environment which can contribute to localizing the excited hole after the exciton dissociation. On the other hand, increasing the oxygen contribution, the semiconductor surfaces can trap both excited electrons and holes at

different crystalline sites. In fact, the (101) and (001) surfaces exhibit a characteristic band-edge for VB which contributes to generate •OH radicals from oxidation mediated by the excited holes trapped on the undercoordinated silver and tungsten clusters. Nonetheless, the (010) surface exhibits a chemical environment with Ag-O-W bond paths where the excited electrons and holes can be dissociated and located at different sites, contributing to both the oxidation and reduction reactions responsible for ROS generation.

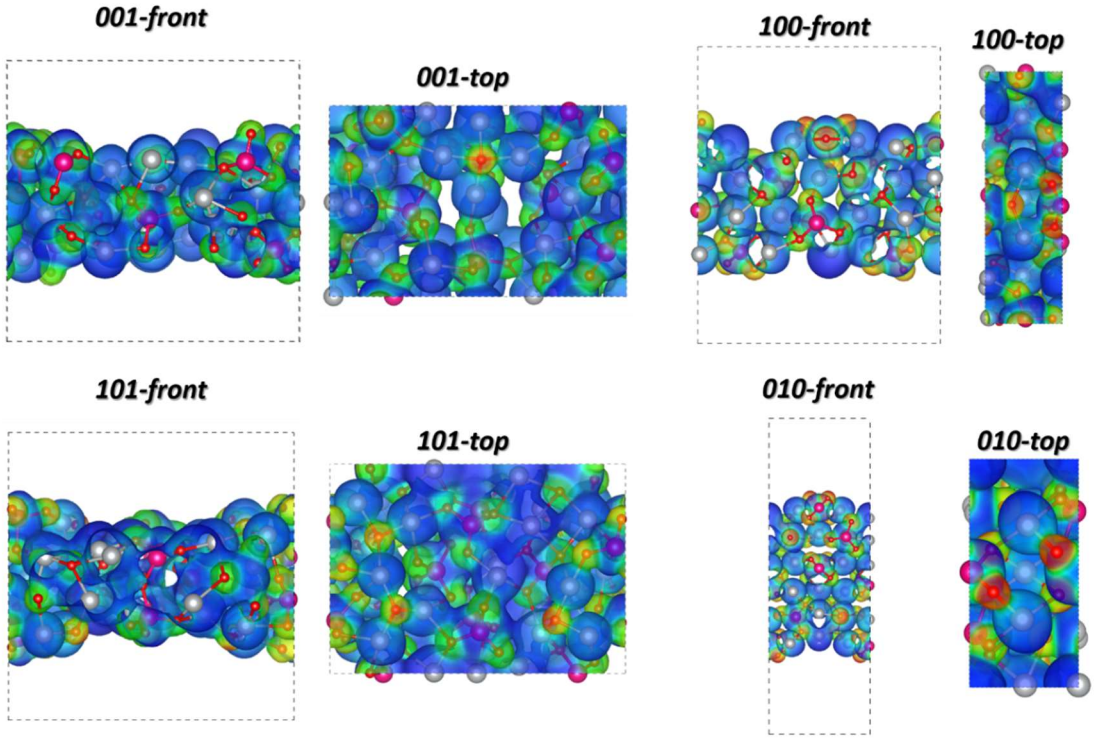


**Figure 5.** Electrostatic potential isosurfaces for (100), (010), (001), and (101) surfaces for α-$Ag_2WO_4$. The blue (red) colors indicate the positive (negative) charge distribution, respectively.

Thus, the electronic structure analysis, combined with the α-$Ag_2WO_4$ surface environment, helps us to rationalize the role of the cross-section morphology in the antimicrobial properties. In addition, the obtained results can also contribute to designing new solid-state materials based on Ag-exposed surfaces for both antimicrobial and antiviral applications.

## 4. Conclusions

This work provides a valuable strategy for understanding how ROS are generated in an α-$Ag_2WO_4$ semiconductor with photoenhanced catalytic and antimicrobial activity. The temperature variation in the co-precipitation synthesis was efficient in controlling the cross-section of the α-$Ag_2WO_4$ rods. The diffractograms also showed that there was no formation of secondary phases, confirming the efficiency of this method in obtaining α-$Ag_2WO_4$ particles. The cross-section variation in the α-$Ag_2WO_4$ sticks did not show significant differences in the antimicrobial tests. *Escherichia coli* bacteria were completely inhibited at concentrations of 2.5–5 mg/mL for both samples, while only a concentration of 5 mg/mL completely inhibited *Salmonella* spp. growth. These low α-$Ag_2WO_4$ concentrations indicate that both cross-sections are efficient for treating environments that contain such bacteria. The theoretical results based on DFT calculations confirmed that the bulk and (010) and surfaces are responsible for the biological activity due to the band-edge position in ROS generation and cation distribution along the exposed surfaces, which contributes to enhancing the reactivity and biological response.

**Supplementary Materials:** The following supporting information can be downloaded at: https://www.mdpi.com/article/10.3390/applnano4030012/s1, Figure S1: Minimal inhibitory concentration (MIC) for AW30 (B, C, and D) and AW70 (E, F, and G) samples against E. coli.; Figure S2. Minimal inhibitory concentration (MIC) for AW30 (B, C, and D) and AW70 (E, F, and G) samples against *Salmonella* spp.; Figure S3. Experimental results for optical band-gap of AW30 (a) and AW70 (b) samples; Table S1. Fractional coordinates obtained by the Rietveld refinement.

**Author Contributions:** Conceptualization, N.F.A.N., J.H.O.N., E.L., M.R.D.B. and F.V.M.; Data curation, N.F.A.N., J.H.O.N., M.R.D.B. and F.V.M.; Formal Analysis, N.F.A.N., M.C.O. and R.A.P.R.; Validation, N.F.A.N., M.C.O. and R.A.P.R.; Visualization, N.F.A.N., M.C.O. and R.A.P.R.; Writing—original draft, N.F.A.N., M.C.O. and R.A.P.R.; Writing—review & editing, N.F.A.N., M.C.O. and R.A.P.R.; Project Administration, N.F.A.N., J.H.O.N., M.C.O., R.A.P.R., M.R.D.B. and F.V.M.; Funding acquisition, E.L., M.R.D.B. and F.V.M.; Supervision, J.H.O.N., M.R.D.B. and F.V.M. All authors have read and agreed to the published version of the manuscript.

**Funding:** This study was partly financed by the *Coordenação de Aperfeiçoamento de Pessoal de Nível Superior—Brasil* (CAPES/PROCAD)—Finance Code 2013/2998/2014, and the authors also acknowledge the financial support from the Brazilian research financing institution: CNPq No. 307546/2014. E. Longo and M. C. Oliveira acknowledge the financial support from *FAPESP* under grants 2013/07296-2 and 2021/01651-1. The authors also thank the National Laboratory for Scientific Computing (LNCC) and the High-Performance Computing Center (NACAD) at the Federal University of Rio de Janeiro (COPPE-UFRJ) for providing the computational resources of the Lobo Carneiro supercomputer. R. A. P. Ribeiro is grateful for the financial assistance from FAPEMIG (project no. APQ-00079-21) and UEMG for the Productivity Program.

**Data Availability Statement:** The data that support the findings of this study are available from the corresponding author, upon reasonable request.

**Conflicts of Interest:** The authors declare no conflict of interest.

## References

1. Bullington, W.; Hempstead, S.; Smyth, A.R.; Drevinek, P.; Saiman, L.; Waters, V.J.; Bell, S.C.; VanDevanter, D.R.; Flume, P.A.; Elborn, S.; et al. Antimicrobial resistance: Concerns of healthcare providers and people with CF. *J. Cyst. Fibros.* **2021**, *20*, 407–412. [CrossRef] [PubMed]
2. Tan, P.; Fu, H.; Ma, X. Design, optimization, and nanotechnology of antimicrobial peptides: From exploration to applications. *Nano Today* **2021**, *39*, 101229. [CrossRef]
3. Martins, L.; Gonçalves, J.L.; Leite, R.F.; Tomazi, T.; Rall, V.L.M.; Santos, M.V. Association between antimicrobial use and antimicrobial resistance of Streptococcus uberis causing clinical mastitis. *J. Dairy Sci.* **2021**, *104*, 12030–12041. [CrossRef] [PubMed]
4. Laird, T.J.; Abraham, S.; Jordan, D.; Pluske, J.R.; Hampson, D.J.; Trott, D.J.; O'Dea, M. Porcine enterotoxigenic Escherichia coli: Antimicrobial resistance and development of microbial-based alternative control strategies. *Vet. Microbiol.* **2021**, *258*, 109117. [CrossRef] [PubMed]
5. Ekinci, S.; İlter, Z.; Ercan, S.; Çınar, E.; Çakmak, R. Magnetite nanoparticles grafted with murexide-terminated polyamidoamine dendrimers for removal of lead (II) from aqueous solution: Synthesis, characterization, adsorption and antimicrobial activity studies. *Heliyon* **2021**, *7*, e06600. [CrossRef]
6. Sharmin, S.; Rahaman, M.M.; Sarkar, C.; Atolani, O.; Islam, M.T.; Adeyemi, O.S. Nanoparticles as antimicrobial and antiviral agents: A literature-based perspective study. *Heliyon* **2021**, *7*, e06456. [CrossRef]
7. Vidhya, E.; Vijayakumar, S.; Nilavukkarasi, M.; Punitha, V.N.; Snega, S.; Praseetha, P.K. Green fabricated MgO nanoparticles as antimicrobial agent: Characterization and evaluation. *Mater. Today Proc.* **2021**, *45*, 5579–5583. [CrossRef]
8. Behzadinasab, S.; Chin, A.; Hosseini, M.; Poon, L.; Ducker, W.A. A Surface Coating that Rapidly Inactivates SARS-CoV-2. *ACS Appl. Mater. Interfaces* **2020**, *12*, 34723–34727. [CrossRef]
9. Assis, M.; de Foggi, C.C.; Teodoro, V.; de Campos da Costa, J.P.; Silva, C.E.; Robeldo, T.; Caperucci, P.F.; Vergani, C.E.; Borra, R.C.; Sorribes, I.; et al. Surface-dependent photocatalytic and biological activities of $Ag_2CrO_4$: Integration of experiment and simulation. *Appl. Surf. Sci.* **2021**, *545*, 148964. [CrossRef]
10. Pinatti, I.M.; Tello, A.C.M.; Trench, A.B.; de Foggi, C.C.; Pereira, P.F.S.; Teixeira, M.M.; Jacomaci, N.; Andrés, J.; Longo, E. Zinc-substituted $Ag_2CrO_4$: A material with enhanced photocatalytic and biological activity. *J. Alloys Compd.* **2020**, *835*, 155315. [CrossRef]
11. Laier, L.O.; Assis, M.; Foggi, C.C.; Gouveia, A.F.; Vergani, C.E.; Santana, L.C.L.; Cavalcante, L.S.; Andrés, J.; Longo, E. Surface-dependent properties of $\alpha$-$Ag_2WO_4$: A joint experimental and theoretical investigation. *Theor. Chem. Acc.* **2020**, *139*, 108. [CrossRef]

12. Alvarez-Roca, R.; Gouveia, A.F.; de Foggi, C.C.; Lemos, P.S.; Gracia, L.; da Silva, L.F.; Vergani, C.E.; San-Miguel, M.; Longo, E.; Andrés, J. Selective Synthesis of α-, β-, and γ-$Ag_2WO_4$ Polymorphs: Promising Platforms for Photocatalytic and Antibacterial Materials. *Inorg. Chem.* **2021**, *60*, 1062–1079. [CrossRef]
13. Foggi, C.C.; Fabbro, M.T.; Santos, L.P.S.; de Santana, Y.V.B.; Vergani, C.E.; Machado, A.L.; Cordoncillo, E.; Andrés, J.; Longo, E. Synthesis and evaluation of α-$Ag_2WO_4$ as novel antifungal agent. *Chem. Phys. Lett.* **2017**, *674*, 125–129. [CrossRef]
14. de Foggi, C.C.; de Oliveira, R.C.; Fabbro, M.T.; Vergani, C.E.; Andres, J.; Longo, E.; Machado, A.L. Tuning the Morphological, Optical, and Antimicrobial Properties of α-$Ag_2WO_4$ Microcrystals Using Different Solvents. *Cryst. Growth Des.* **2017**, *17*, 6239–6246. [CrossRef]
15. Cruz-Filho, J.F.; Costa, T.M.S.; Lima, M.S.; Nolêto, L.F.G.; Bandeira, C.C.S.; Lima, F.L.; Luz, G.E. Microorganisms Photocatalytic Inactivation on $Ag_3PO_4$ Sub-Microcrystals Under WLEDs Light Source. *J. Inorg. Organomet. Polym. Mater.* **2021**, *31*, 2233–2241. [CrossRef]
16. Ribeiro, L.K.; Assis, M.; Lima, L.R.; Coelho, D.; Gonçalves, M.O.; Paiva, R.S.; Moraes, L.N.; Almeida, L.F.; Lipsky, F.; San-Miguel, M.A.; et al. Bioactive $Ag_3PO_4$/Polypropylene Composites for Inactivation of SARS-CoV-2 and Other Important Public Health Pathogens. *J. Phys. Chem. B* **2021**, *125*, 10866–10875. [CrossRef]
17. de Oliveira, R.C.; de Foggi, C.C.; Teixeira, M.M.; da Silva, M.D.P.; Assis, M.; Francisco, E.M.; Pimentel, B.N.A.d.S.; Pereira, P.F.d.S.; Vergani, C.E.; Machado, A.L.; et al. Mechanism of Antibacterial Activity via Morphology Change of α-$AgVO_3$: Theoretical and Experimental Insights. *ACS Appl. Mater. Interfaces* **2017**, *9*, 11472–11481. [CrossRef]
18. Moura, J.V.B.; Freitas, T.S.; Cruz, R.P.; Pereira, R.L.S.; Silva, A.R.P.; Santos, A.T.L.; da Silva, J.H.; Luz-Lima, C.; Freire, P.T.C.; Coutinho, H.D.M. β-$Ag_2MoO_4$ microcrystals: Characterization, antibacterial properties and modulation analysis of antibiotic activity. *Biomed. Pharmacother.* **2017**, *86*, 242–247. [CrossRef]
19. Oliveira, C.A.; Volanti, D.P.; Nogueira, A.E.; Zamperini, C.A.; Vergani, C.E.; Longo, E. Well-designed β-$Ag_2MoO_4$ crystals with photocatalytic and antibacterial activity. *Mater. Des.* **2017**, *115*, 73–81. [CrossRef]
20. Fabbro, M.T.; Foggi, C.C.; Santos, L.P.S.; Gracia, L.; Perrin, A.; Perrin, C.; Vergani, C.E.; Machado, A.L.; Andrés, J.; Cordoncillo, E.; et al. Synthesis, antifungal evaluation and optical properties of silver molybdate microcrystals in different solvents: A combined experimental and theoretical study. *Dalton Trans.* **2016**, *45*, 10736–10743. [CrossRef]
21. De Foggi, C.C.; De Oliveira, R.C.; Assis, M.; Fabbro, M.T.; Mastelaro, V.R.; Vergani, C.E.; Gracia, L.; Andrés, J.; Longo, E.; Machado, A.L. Unvealing the role of β-$Ag_2MoO_4$ microcrystals to the improvement of antibacterial activity. *Mater. Sci. Eng. C* **2020**, *111*, 110765. [CrossRef] [PubMed]
22. Yin, H.; Zhang, M.; Yao, J.; Luo, Y.; Li, P.; Liu, X.; Chen, S. Surfactant-assisted synthesis of direct Z-scheme AgBr/β-$Ag_2WO_4$ heterostructures with enhanced visible-light-driven photocatalytic activities. *Mater. Sci. Semicond. Process.* **2020**, *105*, 104688. [CrossRef]
23. Longo, V.M.; De Foggi, C.C.; Ferrer, M.M.; Gouveia, A.F.; André, R.S.; Avansi, W.; Vergani, C.E.; Machado, A.L.; Andrés, J.; Cavalcante, L.S.; et al. Potentiated Electron Transference in α-$Ag_2WO_4$ Microcrystals with Ag Nanofilaments as Microbial Agent. *J. Phys. Chem. A* **2014**, *118*, 5769–5778. [CrossRef] [PubMed]
24. Assis, M.; Robeldo, T.; Foggi, C.C.; Kubo, A.M.; Mínguez-Vega, G.; Condoncillo, E.; Beltran-Mir, H.; Torres-Mendieta, R.; Andrés, J.; Oliva, M.; et al. Ag Nanoparticles/α-$Ag_2WO_4$ Composite Formed by Electron Beam and Femtosecond Irradiation as Potent Antifungal and Antitumor Agents. *Sci. Rep.* **2019**, *9*, 9927. [CrossRef]
25. Macedo, N.G.; Machado, T.R.; Roca, R.A.; Assis, M.; Foggi, C.C.; Puerto-Belda, V.; Mínguez-Vega, G.; Rodrigues, A.; San-Miguel, M.A.; Cordoncillo, E.; et al. Tailoring the Bactericidal Activity of Ag Nanoparticles/α-$Ag_2WO_4$ Composite Induced by Electron Beam and Femtosecond Laser Irradiation: Integration of Experiment and Computational Modeling. *ACS Appl. Bio Mater.* **2019**, *2*, 824–837. [CrossRef]
26. Haro Chávez, N.L.; de Avila, E.D.; Barbugli, P.A.; de Oliveira, R.C.; de Foggi, C.C.; Longo, E.; Vergani, C.E. Promising effects of silver tungstate microcrystals on fibroblast human cells and three dimensional collagen matrix models: A novel non-cytotoxic material to fight oral disease. *Colloids Surf. B Biointerfaces* **2018**, *170*, 505–513. [CrossRef]
27. Wang, B.-Y.; Zhang, G.-Y.; Cui, G.-W.; Xu, Y.-Y.; Liu, Y.; Xing, C.-Y. Controllable fabrication of α-$Ag_2WO_4$ nanorod-clusters with superior simulated sunlight photocatalytic performance. *Inorg. Chem. Front.* **2019**, *6*, 209–219. [CrossRef]
28. Toby, B. EXPGUI, a graphical user interface for GSAS. *J. Appl. Crystallogr.* **2001**, *34*, 210–213. [CrossRef]
29. Wiegand, I.; Hilpert, K.; Hancock, R.E.W. Agar and broth dilution methods to determine the minimal inhibitory concentration (MIC) of antimicrobial substances. *Nat. Protoc.* **2008**, *3*, 163–175. [CrossRef]
30. Dovesi, R.; Erba, A.; Orlando, R.; Zicovich-Wilson, C.M.; Civalleri, B.; Maschio, L.; Rérat, M.; Casassa, S.; Baima, J.; Salustro, S.; et al. Quantum-mechanical condensed matter simulations with CRYSTAL. *Wiley Interdiscip. Rev. Comput. Mol. Sci.* **2018**, *8*, e1360. [CrossRef]
31. Becke, A.D. Density-functional exchange-energy approximation with correct asymptotic behavior. *Phys. Rev. A* **1988**, *38*, 3098–3100. [CrossRef]
32. Lee, C.; Yang, W.; Parr, R.G. Development of the Colle-Salvetti correlation-energy formula into a functional of the electron density. *Phys. Rev. B* **1988**, *37*, 785–789. [CrossRef]
33. Assis, M.; Pontes Ribeiro, R.A.; Carvalho, M.H.; Teixeira, M.M.; Gobato, Y.G.; Prando, G.A.; Mendonça, C.R.; de Boni, L.; Aparecido de Oliveira, A.J.; Bettini, J.; et al. Unconventional Magnetization Generated from Electron Beam and Femtosecond Irradiation on α-$Ag_2WO_4$: A Quantum Chemical Investigation. *ACS Omega* **2020**, *5*, 10052–10067. [CrossRef]

34. Longo, E.; Volanti, D.P.; Longo, V.M.; Gracia, L.; Nogueira, I.C.; Almeida, M.A.P.; Pinheiro, A.N.; Ferrer, M.M.; Cavalcante, L.S.; Andrés, J. Toward an Understanding of the Growth of Ag Filaments on α-$Ag_2WO_4$ and Their Photoluminescent Properties: A Combined Experimental and Theoretical Study. *J. Phys. Chem. C* **2014**, *118*, 1229–1239. [CrossRef]
35. Trench, A.B.; Machado, T.R.; Gouveia, A.F.; Assis, M.; da Trindade, L.G.; Santos, C.; Perrin, A.; Perrin, C.; Oliva, M.; Andrés, J.; et al. Connecting structural, optical, and electronic properties and photocatalytic activity of $Ag_3PO_4$:Mo complemented by DFT calculations. *Appl. Catal. B Environ.* **2018**, *238*, 198–211. [CrossRef]
36. Lemos, P.S.; Altomare, A.; Gouveia, A.F.; Nogueira, I.C.; Gracia, L.; Llusar, R.; Andrés, J.; Longo, E.; Cavalcante, L.S. Synthesis and characterization of metastable β-$Ag_2WO_4$: An experimental and theoretical approach. *Dalton Trans.* **2016**, *45*, 1185–1191. [CrossRef]
37. Pereira, P.F.S.; Santos, C.C.; Gouveia, A.F.; Ferrer, M.M.; Pinatti, I.M.; Botelho, G.; Sambrano, J.R.; Rosa, I.L.V.; Andrés, J.; Longo, E. α-Ag2–2xZnxWO4 ($0 \leq x \leq 0.25$) Solid Solutions: Structure, Morphology, and Optical Properties. *Inorg. Chem.* **2017**, *56*, 7360–7372. [CrossRef]
38. Aprà, E.; Stefanovich, E.; Dovesi, R.; Roetti, C. An ab initio Hartree—Fock study of silver chloride. *Chem. Phys. Lett.* **1991**, *186*, 329–335. [CrossRef]
39. Corà, F.; Patel, A.; Harrison, N.M.; Dovesi, R.; Catlow, C.R.A. An ab Initio Hartree−Fock Study of the Cubic and Tetragonal Phases of Bulk Tungsten Trioxide. *J. Am. Chem. Soc.* **1996**, *118*, 12174–12182. [CrossRef]
40. Mackrodt, W.C.; Harrison, N.M.; Saunders, V.R.; Allan, N.L.; Towler, M.D.; Aprà, E.; Dovesi, R. Ab initio Hartree-Fock calculations of CaO, VO, MnO and NiO. *Philos. Mag. A* **1993**, *68*, 653–666. [CrossRef]
41. Macedo, N.G.; Gouveia, A.F.; Roca, R.A.; Assis, M.; Gracia, L.; Andrés, J.; Leite, E.R.; Longo, E. Surfactant-Mediated Morphology and Photocatalytic Activity of α-$Ag_2WO_4$ Material. *J. Phys. Chem. C* **2018**, *122*, 8667–8679. [CrossRef]
42. Roca, R.A.; Sczancoski, J.C.; Nogueira, I.C.; Fabbro, M.T.; Alves, H.C.; Gracia, L.; Santos, L.P.S.; de Sousa, C.P.; Andrés, J.; Luz, G.E.; et al. Facet-dependent photocatalytic and antibacterial properties of α-$Ag_2WO_4$ crystals: Combining experimental data and theoretical insights. *Catal. Sci. Technol.* **2015**, *5*, 4091–4107. [CrossRef]
43. Pirhashemi, M.; Habibi-Yangjeh, A. Preparation of novel nanocomposites by deposition of $Ag_2WO_4$ and AgI over ZnO particles: Efficient plasmonic visible-light-driven photocatalysts through a cascade mechanism. *Ceram. Int.* **2017**, *43*, 13447–13460. [CrossRef]
44. Andrade Neto, N.F.; Oliveira, P.M.; Bomio, M.R.D.; Motta, F.V. Effect of temperature on the morphology and optical properties of $Ag_2WO_4$ obtained by the co-precipitation method: Photocatalytic activity. *Ceram. Int.* **2019**, *45*, 15205–15212. [CrossRef]
45. Shaker-Agjekandy, S.; Habibi-Yangjeh, A. Facile one-pot method for preparation of AgI/ZnO nanocomposites as visible-light-driven photocatalysts with enhanced activities. *Mater. Sci. Semicond. Process.* **2015**, *34*, 74–81. [CrossRef]
46. Nobre, F.X.; Bastos, I.S.; dos Santos Fontenelle, R.O.; Júnior, E.A.A.; Takeno, M.L.; Manzato, L.; de Matos, J.M.E.; Orlandi, P.P.; de Fátima Souza Mendes, J.; Brito, W.R.; et al. Antimicrobial properties of α-$Ag_2WO_4$ rod-like microcrystals synthesized by sonochemistry and sonochemistry followed by hydrothermal conventional method. *Ultrason. Sonochem.* **2019**, *58*, 104620. [CrossRef]
47. Assis, M.; Cordoncillo, E.; Torres-Mendieta, R.; Beltrán-Mir, H.; Mínguez-Vega, G.; Oliveira, R.; Leite, E.R.; Foggi, C.C.; Vergani, C.E.; Longo, E.; et al. Towards the scale-up of the formation of nanoparticles on α-$Ag_2WO_4$ with bactericidal properties by femtosecond laser irradiation. *Sci. Rep.* **2018**, *8*, 1884. [CrossRef]
48. Li, D.; Chen, S.; Zhang, K.; Gao, N.; Zhang, M.; Albasher, G.; Shi, J.; Wang, C. The interaction of $Ag_2O$ nanoparticles with Escherichia coli: Inhibition–sterilization process. *Sci. Rep.* **2021**, *11*, 1703. [CrossRef]
49. Wang, X.; Wu, H.-F.; Kuang, Q.; Huang, R.-B.; Xie, Z.-X.; Zheng, L.-S. Shape-Dependent Antibacterial Activities of $Ag_2O$ Polyhedral Particles. *Langmuir* **2010**, *26*, 2774–2778. [CrossRef]
50. Assis, M.; Simoes, L.G.P.; Tremiliosi, G.C.; Coelho, D.; Minozzi, D.T.; Santos, R.I.; Vilela, D.C.B.; Santos, J.R.d.; Ribeiro, L.K.; Rosa, I.L.V.; et al. $SiO_2$-Ag Composite as a Highly Virucidal Material: A Roadmap that Rapidly Eliminates SARS-CoV-2. *Nanomaterials* **2021**, *11*, 638. [CrossRef]
51. Mosselhy, D.A.; Kareinen, L.; Kivistö, I.; Aaltonen, K.; Virtanen, J.; Ge, Y.; Sironen, T. Copper-Silver Nanohybrids: SARS-CoV-2 Inhibitory Surfaces. *Nanomaterials* **2021**, *11*, 1820. [CrossRef] [PubMed]
52. Hosseini, M.; Chin, A.W.H.; Behzadinasab, S.; Poon, L.L.M.; Ducker, W.A. Cupric Oxide Coating That Rapidly Reduces Infection by SARS-CoV-2 via Solids. *ACS Appl. Mater. Interfaces* **2021**, *13*, 5919–5928. [CrossRef] [PubMed]
53. Wang, D.; Zhao, L.; Wang, D.; Yan, L.; Jing, C.; Zhang, H.; Guo, L.-H.; Tang, N. Direct evidence for surface long-lived superoxide radicals photo-generated in $TiO_2$ and other metal oxide suspensions. *Phys. Chem. Chem. Phys.* **2018**, *20*, 18978–18985. [CrossRef] [PubMed]
54. Yao, H.; Huang, Y.; Li, X.; Li, X.; Xie, H.; Luo, T.; Chen, J.; Chen, Z. Underlying mechanisms of reactive oxygen species and oxidative stress photoinduced by graphene and its surface-functionalized derivatives. *Environ. Sci. Nano* **2020**, *7*, 782–792. [CrossRef]
55. Lacerda, L.H.d.S.; San-Miguel, M.A. DFT approaches unraveling the surface and morphological properties of $MnMoO_4$. *Appl. Surf. Sci.* **2021**, *567*, 150882. [CrossRef]
56. Nosaka, Y.; Nosaka, A.Y. Generation and Detection of Reactive Oxygen Species in Photocatalysis. *Chem. Rev.* **2017**, *117*, 11302–11336. [CrossRef] [PubMed]

57. Schwarz, H.A.; Dodson, R.W. Equilibrium between hydroxyl radicals and thallium(II) and the oxidation potential of hydroxyl(aq). *J. Phys. Chem.* **1984**, *88*, 3643–3647. [CrossRef]
58. Gouveia, A.F.; Gracia, L.; Longo, E.; San-Miguel, M.A.; Andrés, J. Modulating the properties of multifunctional semiconductors by means of morphology: Theory meets experiments. *Comput. Mater. Sci.* **2021**, *188*, 110217. [CrossRef]
59. Ribeiro, R.A.P.; Oliveira, M.C.; Bomio, M.R.D.; de Lazaro, S.R.; Andrés, J.; Longo, E. Connecting the surface structure, morphology and photocatalytic activity of $Ag_2O$: An in depth and unified theoretical investigation. *Appl. Surf. Sci.* **2020**, *509*, 145321. [CrossRef]
60. da Costa Borges Soares, M.; Barbosa, F.F.; Torres, M.A.M.; Valentini, A.; dos Reis Albuquerque, A.; Sambrano, J.R.; Pergher, S.B.C.; Essayem, N.; Braga, T.P. Oxidative dehydrogenation of ethylbenzene to styrene over the $CoFe_2O_4$–MCM-41 catalyst: Preferential adsorption on the $O^{2-}Fe^{3+}O^{2-}$ sites located at octahedral positions. *Catal. Sci. Technol.* **2019**, *9*, 2469–2484. [CrossRef]
61. Amoresi, R.A.C.; Oliveira, R.C.; Marana, N.L.; de Almeida, P.B.; Prata, P.S.; Zaghete, M.A.; Longo, E.; Sambrano, J.R.; Simões, A.Z. $CeO_2$ Nanoparticle Morphologies and Their Corresponding Crystalline Planes for the Photocatalytic Degradation of Organic Pollutants. *ACS Appl. Nano Mater.* **2019**, *2*, 6513–6526. [CrossRef]